

Echoes from hairy black holes

Guangzhou Guo,^a Peng Wang,^a Houwen Wu^{a,b} and Haitang Yang^a

^a*Center for Theoretical Physics, College of Physics, Sichuan University,
Yihuan Road, Chengdu, 610065, China*

^b*Department of Applied Mathematics and Theoretical Physics, University of Cambridge,
Wilberforce Road, Cambridge, CB3 0WA, U.K.*

E-mail: gzguo@stu.scu.edu.cn, pengw@scu.edu.cn, hw598@damtp.cam.ac.uk,
hyanga@scu.edu.cn

ABSTRACT: We study the waveforms of time signals produced by scalar perturbations in static hairy black holes, in which the perturbations can be governed by a double-peak effective potential. The inner potential peak would give rise to echoes, which provide a powerful tool to test the Kerr hypothesis. The waveforms are constructed in the time and frequency domains, and we find that the late-time waveforms are determined by the long-lived and sub-long-lived quasinormal modes, which are trapped in the potential valley and near the smaller peak, respectively. When the distance between the peaks is significantly larger than the width of the peaks, a train of decaying echo pulses is produced by the superposition of the long-lived and sub-long-lived modes. In certain cases, the echoes can vanish and then reappear. When the peaks are close enough, one detects far fewer echo signals and a following sinusoid tail, which is controlled by the long-lived or sub-long-lived mode and hence decays very slowly.

KEYWORDS: Black Holes, Classical Theories of Gravity

ARXIV EPRINT: [2204.00982](https://arxiv.org/abs/2204.00982)

Contents

1	Introduction	1
2	Set up	3
2.1	Hairy black holes	3
2.2	Time-dependent scalar field perturbations	4
3	Numerical results	6
3.1	Single-peak potential	7
3.2	Wormhole-like potential	8
3.3	Adjacent double-peak potential	10
4	Conclusions	13

1 Introduction

The existence of black holes in the universe is one of the most prominent predictions of general relativity. Owing to advanced observation techniques developed in the past decade, we are capable of exploring the nature of black holes and testing general relativity in the strong field regime. Gravitational waves from a binary black hole merger were successfully detected by LIGO and Virgo [1], and subsequently the first image of a supermassive black hole at the center of galaxy M87 was photographed by the Event Horizon Telescope [2–7], which opens a new era of black hole physics. Specifically, the ringdown waveforms of gravitational waves are characterized by quasinormal modes of final black holes [8–10], and hence the measurements of the ringdown waveforms offer new opportunities to probe the detailed properties of black hole spacetime, e.g., the black hole mass and spin [11, 12].

Although current observations are found to be in good agreement with the predictions of general relativity, observational uncertainties still leave some room for alternatives to the Kerr black hole. In particular, horizonless exotic compact objects (ECOs), e.g., boson stars, gravastars and wormholes, have attracted a lot of attentions [13–23]. Intriguingly, echo signals associated with the post-merger ringdown phase in the binary black hole waveforms can be found in various ECO models [10, 24–31]. Moreover, the recent LIGO/Virgo data may show the potential evidence of echoes in gravitational wave waveforms of binary black hole mergers [32, 33]. As anticipated, echoes are closely related to quasinormal modes [11, 24, 34]. Specifically, it was argued that echoes are dominated by long-lived quasinormal modes of ECOs, and the echo waveforms can be accurately reconstructed from the quasinormal modes [24]. Moreover, quasinormal modes of ECOs can be extracted from echo signals by a Prony method [9, 35], which can be used to approximately reconstruct effective potentials of the ECO spacetime [36]. To gain a deeper insight into the generation

of echoes, a reflecting boundary was placed in a black hole spacetime to mimic ECOs, and it showed that the reflecting boundary plays a central role in producing extra time-delay echo pluses, which constitute the echo waveform received by a distant observer [37]. This observation implies that echoes are expected to occur in the spacetime with a double-peak effective scattering potential (e.g., wormholes), where the inner potential peak acts as a reflecting boundary.

Contrary to the common lore that detections of echoes in late-time ringdown signals can be used to distinguish black holes with wormholes, echo signals have been reported in several black hole models, e.g., quantum black holes [38–42], black holes with discontinuous effective potentials [43], nonuniform area quantization on black hole [44] and gravitons with modified dispersion relations [45]. Remarkably, much less radical proposals for echoes from black holes do exist in the literature. In fact, echoes have been found in dyonic black holes with a quasi-topological electromagnetic term, which have multiple photon spheres and double-peak effective potentials [46, 47]. In a black hole of massive gravity, gravitational perturbations should couple with the background metric and Stuckelberg fields, which could give echo signals in the gravitational waves [48–50]. Given the theoretical and observational importance of echoes, it is of great significance to find more black hole spacetimes that can produce echo signals.

Recently, a novel type of hairy black hole solutions were constructed in Einstein-Maxwell-scalar (EMS) models [51–55], which serve as counter-examples to the no-hair theorem [56–58]. In the EMS models, the scalar field is non-minimally coupled to the electromagnetic field and can trigger a tachyonic instability to form spontaneously scalarized hairy black holes from Reissner-Nordström (RN) black holes. Properties of the hairy black holes have been extensively studied in the literature, e.g., different non-minimal coupling functions [59–61], massive and self-interacting scalar fields [62, 63], horizonless reflecting stars [64], stability analysis of hairy black holes [65–69], higher dimensional scalar-tensor models [70], quasinormal modes of hairy black holes [71, 72], two U(1) fields [73], quasi-topological electromagnetism [74], topology and spacetime structure influences [75], scalarized black holes in the dS/AdS spacetime [54, 76–78], perturbations of stealth black holes with a linearly evolving hair [79], and circular black hole solutions [80].

In recent works [81, 82], we found that the hairy black holes can also possess multiple photon spheres outside the event horizon, which have significant effects on the optical observation of black holes illuminated by the surrounding accretion disk, e.g., leading to bright rings of different radii in the black hole images [81] and significantly increasing the flux of the observed images [82]. Later, it showed that the effective potential for a scalar perturbation in the hairy black holes exhibits a double-peak structure [83]. In the eikonal limit, the extrema of the double-peak potential correspond to the photon spheres, around which long-lived and sub-long-lived quasinormal modes were found [83]. The appearance of the double-peak effective potentials naturally motivates us to search echo signals of perturbations in the hairy black holes. Moreover, it is highly desirable to explore the relationship between echoes and the long-lived and sub-long-lived modes obtained in [83]. To this end, we numerically obtain time-domain echoes of scalar perturbations in the hairy black holes and reconstruct the late-time signals from associated quasinormal modes in

this paper. The remainder of this paper is organized as follows. In section 2, after the hairy black hole solution is briefly reviewed, we consider a time-dependent scalar field perturbation propagating in the hairy black holes and relate it to the quasinormal mode spectrum. The evolutions of the scalar field perturbation in different profiles of effective potentials are exhibited in section 3. We finally conclude our main results in section 4. We set $16\pi G = 1$ throughout this paper.

2 Set up

In this section, we first briefly review spherically symmetric hairy black hole solutions in the EMS model. In the hairy black hole background, the evolution of time-dependent scalar perturbations from initial data is then studied and related to the corresponding quasinormal modes.

2.1 Hairy black holes

The scalar field ϕ is minimally coupled to the metric field and non-minimally coupled to the electromagnetic field A_μ in the EMS model, which is described by the action

$$S = \int d^4x \sqrt{-g} \left[R - 2(\partial\phi)^2 - e^{\alpha\phi^2} F^2 \right]. \quad (2.1)$$

Here, $F_{\mu\nu} = \partial_\mu A_\nu - \partial_\nu A_\mu$ is the electromagnetic field strength tensor, and $e^{\alpha\phi^2}$ is the coupling function between ϕ and A_μ . With the spherically symmetric and asymptotically flat black hole ansatz [51, 54],

$$ds^2 = -N(r) e^{-2\delta(r)} dt^2 + \frac{1}{N(r)} dr^2 + r^2 (d\theta^2 + \sin^2\theta d\varphi^2),$$

$$A_\mu dx^\mu = V(r) dt \quad \text{and} \quad \phi = \phi(r), \quad (2.2)$$

the equations of motion for the action (2.1) are given by

$$m'(r) = \frac{Q^2}{2r^2 e^{\alpha\phi^2(r)}} + \frac{1}{2} r^2 N(r) \phi'^2(r)$$

$$\left[r^2 N(r) \phi'(r) \right]' = -\frac{\alpha\phi(r) Q^2}{e^{\alpha\phi^2(r)} r^2} - r^3 N(r) \phi'^3(r),$$

$$\delta'(r) = -r \phi'^2(r), \quad (2.3)$$

$$V'(r) = \frac{Q}{r^2 e^{\alpha\phi^2(r)}} e^{-\delta(r)},$$

where primes denote derivatives with respect to r . In the above equations (2.3), the integration constant Q is interpreted as the electric charge of the black hole solution, and the Misner-Sharp mass function $m(r)$ is defined via $N(r) \equiv 1 - 2m(r)/r$.

Black hole solutions of the non-linear ordinary differential equations (2.3) can be obtained as appropriate boundary conditions at the event horizon r_h and the spatial infinity are imposed,

$$m(r_h) = r_h/2, \quad \delta(r_h) = \delta_0, \quad \phi(r_h) = \phi_0, \quad V(r_h) = 0,$$

$$m(\infty) = M, \quad \delta(\infty) = 0, \quad \phi(\infty) = 0, \quad V(\infty) = \Phi, \quad (2.4)$$

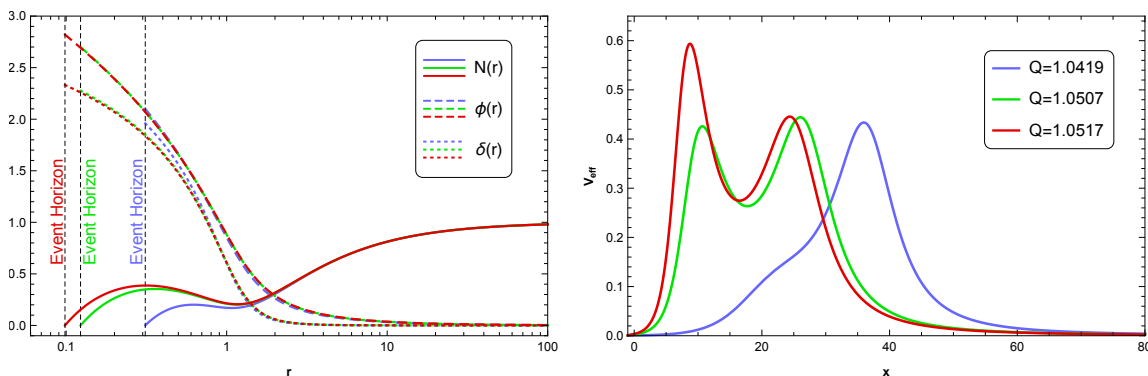


Figure 1. Hairy black hole solutions for $Q = 1.0419$ (blue lines), $Q = 1.0507$ (green lines) and $Q = 1.0517$ (red lines) with $\alpha = 0.8$ and the corresponding $l = 2$ effective potentials of the scalar field. *Left:* the metric functions are plotted outside the event horizon (vertical dashed lines), and the solid, dashed and dotted lines designate $N(r)$, $\phi(r)$ and $\delta(r)$, respectively. *Right:* the effective potentials are displayed against the tortoise coordinate x . For a small value of the charge (e.g., the blue line), the effective potential has only a single extremum. As the black hole charge increases (e.g., the green and red lines), the effective potential presents a double-peak structure with two local maxima and one local minimum.

where Φ is the electrostatic potential, and the black hole mass M is related to the ADM mass. The free parameters δ_0 and ϕ_0 can be used to characterize different black hole solutions. Specifically, $\phi_0 = \delta_0 = 0$ lead to the scalar-free solutions with $\phi = 0$ of eq. (2.3), which are exactly RN black holes. Nevertheless, hairy black hole solutions with a non-trivial scalar field ϕ can exist if non-zero values of ϕ_0 and δ_0 are admitted. In this paper, we set $M = 1$ and use a shooting method built in the *NDSolve* function of *Wolfram* $\text{\textcircled{R}}$ *Mathematica* to numerically solve eq. (2.3) with the given boundary conditions (2.4). The metric functions of three hairy black hole solutions with $\alpha = 0.8$ are exhibited in figure 1, where the blue, green and red lines denote $Q = 1.0419$, $Q = 1.0507$ and $Q = 1.0517$, respectively.

2.2 Time-dependent scalar field perturbations

For a scalar field perturbation $\delta\phi$ around the hairy black hole, the master equation is given by [51, 83]

$$\left[\nabla^\mu \nabla_\mu + \left(\alpha + 2\alpha^2 \phi^2(r) \right) \frac{Q^2}{r^4 e^{\alpha\phi^2(r)}} \right] \delta\phi = 0. \quad (2.5)$$

For later convenience, we define the tortoise coordinate x via $dx/dr \equiv e^{\delta(r)} N^{-1}(r)$. The time-dependent scalar field perturbation $\delta\phi$ can be decomposed in terms of spherical harmonics,

$$\delta\phi = \sum_{l,m} \frac{\psi(t,r)}{r} Y_{lm}(\theta, \varphi). \quad (2.6)$$

With the help of eqs. (2.2) and (2.6), the master equation (2.5) then reduces to

$$\left(-\frac{\partial^2}{\partial t^2} + \frac{\partial^2}{\partial x^2} - V_{\text{eff}}(x) \right) \psi(t, x) = 0, \quad (2.7)$$

where the effective potential $V_{\text{eff}}(x)$ is given by

$$V_{\text{eff}}(x) = \frac{e^{-2\delta(r)}N(r)}{r^2} \left[l(l+1) + 1 - N(r) - \frac{Q^2}{r^2 e^{\alpha\phi(r)^2}} - \left(\alpha + 2\alpha^2\phi(r)^2 \right) \frac{Q^2}{r^2 e^{\alpha\phi(r)^2}} \right]. \quad (2.8)$$

The effective potential with $l = 2$ of various black hole solutions is presented in the right panel of figure 1. Intriguingly, when the black hole charge is large enough, the effective potential can possess a double-peak structure, which consists of two local maxima and one local minimum.

To solve the partial differential equation (2.7), we consider a time-dependent Green's function $G(t, x, x')$, which satisfies

$$\left(-\frac{\partial^2}{\partial t^2} + \frac{\partial^2}{\partial x^2} - V_{\text{eff}}(x) \right) G(t, x, x') = \delta(t) \delta(x - x'). \quad (2.9)$$

One then can express the solution of eq. (2.7) in terms of $G(t, x, x')$ [8, 84],

$$\psi(t, x) = - \int_{-\infty}^{+\infty} [G(t, x, x') \partial_t \psi(0, x') + \partial_t G(t, x, x') \psi(0, x')] dx'. \quad (2.10)$$

Under the Fourier transformation, the solution (2.10) can be rewritten as

$$\psi(t, x) = \frac{1}{2\pi} \int_{-\infty}^{+\infty} \hat{G}(\omega, x, x') \hat{S}(\omega, x) e^{-i\omega t} dx' d\omega, \quad (2.11)$$

where $\hat{S}(\omega, x)$ is determined by the initial data,

$$\hat{S}(\omega, x) = \left[i\omega\psi(t, x) - \frac{\partial\psi(t, x)}{\partial t} \right] \Big|_{t=0}. \quad (2.12)$$

The time-independent Green's function $\hat{G}(\omega, x, x')$ can be constructed in terms of two linearly independent solutions $\hat{\psi}_-(\omega, x)$ and $\hat{\psi}_+(\omega, x)$ to the homogeneous differential equation,

$$\left(\frac{\partial^2}{\partial x^2} + \omega^2 - V_{\text{eff}}(x) \right) \hat{\psi}(\omega, x) = 0, \quad (2.13)$$

with the boundary conditions

$$\begin{aligned} \hat{\psi}_-(\omega, x) &\sim e^{-i\omega x}, & x &\rightarrow -\infty, \\ \hat{\psi}_+(\omega, x) &\sim e^{i\omega x}, & x &\rightarrow +\infty. \end{aligned} \quad (2.14)$$

Particularly, the Green's function $\hat{G}(\omega, x, x')$ is given by

$$\hat{G}(\omega, x, x') = \frac{\hat{\psi}_-(\omega, \min(x, x')) \hat{\psi}_+(\omega, \max(x, x'))}{W(\omega)}, \quad (2.15)$$

where the Wronskian $W(\omega)$ is defined as

$$W(\omega) = \hat{\psi}_-(\omega, x) \partial_x \hat{\psi}_+(\omega, x) - \partial_x \hat{\psi}_-(\omega, x) \hat{\psi}_+(\omega, x). \quad (2.16)$$

When $W(\omega) = 0$, one can infer that $\hat{\psi}_-(\omega, x)$ is identical to $\hat{\psi}_+(\omega, x)$ up to a constant factor, which indicates that $\hat{\psi}_\pm(\omega, x)$ have only ingoing (outgoing) modes at $x = -\infty$ ($x = +\infty$). Therefore, the condition $W(\omega) = 0$ selects a discrete set of quasinormal modes with complex quasinormal frequencies ω_n , where $n = 0, 1, 2 \dots$ is the overtone number.

On the complex plane, the solution $\psi(t, x)$ to eq. (2.7) can be expressed as a sum of quasinormal modes [8],

$$\psi(t, x) = \sum_n \psi_n(t, x) = \sum_n c_n(x) e^{-i\omega_n t}, \quad (2.17)$$

where the coefficient $c_n(x)$ is

$$c_n(x) = \frac{-i}{dW(\omega_n)/d\omega} \int_{-\infty}^{+\infty} \hat{\psi}_-(\omega_n, \min(x, x')) \hat{\psi}_+(\omega_n, \max(x, x')) \hat{S}(\omega_n, x') dx'. \quad (2.18)$$

Since the quasinormal modes come in complex conjugate pairs, the waveform $\psi(t, x)$ given by eq. (2.17) is real as long as the initial data $\hat{S}(\omega_n, x)$ is real [8]. Note that, before the initial data is entirely received by the observer, a time-dependent integration domain in eqs. (2.10) and (2.18) is required to respect causality. Therefore, to well describe the behavior of $\psi(t, x)$ at a early time, the coefficients $c_n(x)$ are argued to depend on time [8, 84]. Nevertheless, we focus on the late-time waveforms throughout this paper, and hence the coefficients $c_n(x)$ are time-independent.

When the real parts of quasinormal frequencies ω_n are an arithmetic progression with regard to the number n ,

$$\text{Re } \omega_n = \omega_0 + \frac{2n\pi}{T}, \quad (2.19)$$

the waveform $\psi(t, x)$ from eq. (2.17) with real initial data then behaves as

$$\psi(t, x) = \sum_n \psi_n(t, x) = 2 \sum_n [\text{Re } c_n \cos(\omega_0 + 2n\pi/T)t + \text{Im } c_n \sin(\omega_0 + 2n\pi/T)t] e^{\text{Im } \omega_n t}, \quad (2.20)$$

where each quasinormal mode $\psi_n(t, x)$ is composed of a complex conjugate pair,

$$\psi_n(t, x) = c_n(x) e^{-i\omega_n t} + c_n^*(x) e^{-i(-\omega_n^*)t}. \quad (2.21)$$

Interestingly, the waveform $\psi(t, x)$ describes damped oscillations with a period T and damping factors, which are the imaginary parts of quasinormal modes. As demonstrated in [24], the inner barrier of a double-peak potential provides a reflecting wall for radiation waves, leading to a set of quasinormal modes in the form of eq. (2.19). Consequently, a distant observer can detect a series of echoes from a double-peak effective potential.

3 Numerical results

In this section, we investigate the waveform $\psi(t, x)$ detected by a distant observer in the hairy black holes with the effective potential of different peak structure. To numerically solve the partial differential equation (2.7), we consider the initial condition,

$$\psi(t, x)|_{t=0} = 0 \text{ and } \left. \frac{\partial \psi(t, x)}{\partial t} \right|_{t=0} = A \exp\left(-\frac{(x-x_0)^2}{2\Delta^2}\right) \quad [28, 85, 86]. \quad (3.1)$$

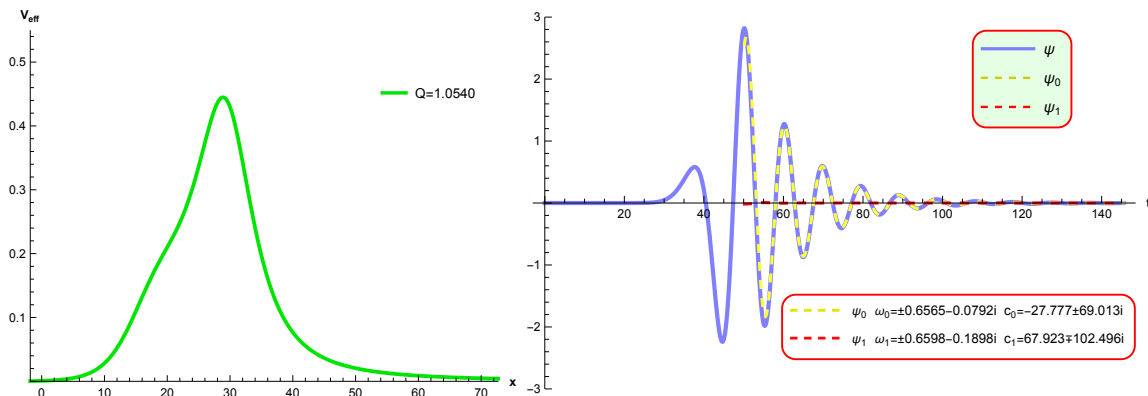


Figure 2. *Left:* the $l = 2$ effective potential of the hairy black hole with $\alpha = 0.9$ and $Q = 1.0540$ as a function of the tortoise coordinate x . The effective potential has a single-peak structure. *Right:* the waveform ψ (blue solid line), and the first and second lowest-lying quasinormal modes ψ_0 (yellow dashed line) and ψ_1 (red dashed line) received by an observer at $x_o = 72.75$. The initial condition is the Gaussian perturbation (3.1) near the peak. The fundamental mode ψ_0 dominates the late-time behavior of the waveform ψ .

In the following numerical simulations, the initial position of the Gaussian wave packet x_0 is placed near the (outer) peak of the effective potential, and the amplitude A and the width Δ are chosen to adapt to the specific case. To check our numerical results and find the frequency content of $\psi(t, x)$, we use eqs. (2.17) and (2.18) to reconstruct the waveform $\psi(t, x)$ at late times from the quasinormal modes. Moreover, we focus on the spherical harmonics of $l = 2$ since they play a dominant role in the ringdown gravitational waves after binary black holes merge [12, 87].

3.1 Single-peak potential

As shown in figure 1, the $l = 2$ effective potential of scalar field perturbations has a single-peak structure when the black hole charge is small enough. In figure 2, we present the evolution of a time-dependent scalar perturbation in the hairy black hole with $\alpha = 0.9$ and $Q = 1.0540$. The $l = 2$ effective potential is plotted in the left panel, which indeed shows a single-peak structure. In the right panel, we display the waveform signal received by an observer at $x_o = 72.75$, who is far away from the potential peak. Specifically, the blue solid line denotes the solution $\psi(t, x_o)$ to the partial differential equation (2.7) with the initial condition (3.1), and the dashed lines represent the low-lying quasinormal modes $\psi_0(t, x_o)$ and $\psi_1(t, x_o)$ obtained from eqs. (2.17), (2.18) and (3.1). Here, we consider the quasinormal modes $\psi_0(t, x_o)$ and $\psi_1(t, x_o)$ only after the initial data is fully received by the observer. The right panel of figure 2 displays that, roughly after the travel time of the initial data from the vicinity of the peak to the observer, the reflection from the potential peak gives an observed burst, which can be accurately reconstructed from ψ_0 and ψ_1 . At late times, the wave signal is dominated by the fundamental quasinormal mode ψ_0 , showing an exponentially damped sinusoid. As expected, due to the absence of the inner peak, no echo is observed after the burst is received. Note that waves propagating on a black

hole spacetime usually develop asymptotically late-time tails, which follow exponentially damped sinusoids and decay as an inverse power of time due to scattering from large radius in the black hole geometry [88, 89]. Nevertheless, discussions on the power-law tails are beyond the scope of the paper.

3.2 Wormhole-like potential

For a large enough black hole charge, there can exist two peaks in the effective potential of scalar field perturbations. Depending on the black hole parameters, the separation between the peaks L can be considerably larger than the Compton wavelength of the scalar field perturbations (or the wavelength of the associated quasinormal modes), which resembles the usual wormhole spacetime. Since the potential peaks are well separated, the scattering of a perturbation off one peak is barely influenced by the other one. The perturbation is reflected off the potential barriers, and bounces back and forth between the two peaks. Meanwhile, the perturbation successively tunnels through the outer barrier, leading to a series of echoes received by a distant observer. In this case, the geometric optics approximation is valid, and hence the time delay between the echoes is roughly $2L$. For a detail discussion, one can refer to [24, 37]. As noted in [24], the appearance of echoes in a double-peak potential is closely related to quasinormal modes residing in the valley between the peaks. When the distance between the peaks is much larger than the width of the peaks, there exists a series of these quasinormal modes, whose imaginary parts are much smaller than their real parts. Similar to a beat produced by multiple sounds of slightly different frequencies, the superposition of the quasinormal modes, which leak through the outer potential barrier, produce approximately periodical echo signals.

In figure 3, we present the numerically computed and reconstructed time signals received by an observer far away from the outer peak of the effective potential in the hairy black hole with $\alpha = 0.52$ and $Q = 1.0074$. The blue line designates the numerical solution $\psi(t, x)$ to the partial differential equation (2.7), while the yellow line represents the sum over the associated quasinormal modes from $n = 0$ to $n = 17$. One can observe that a series of echoes roughly separated by a distance $2L \approx 156.68$ arises at late times, and the sum of quasinormal modes perfectly reconstruct the echoes. In table 1, we list the quasinormal frequency ω_n and the corresponding coefficient c_n for each quasinormal mode ψ_n . Roughly speaking, these quasinormal frequencies ω_n satisfy the form in eq. (2.19) with a period $T \approx 179.52 \sim 2L$, which is consistent with the echo period. To illustrate the contributions from quasinormal modes, the dominant modes $\psi_9 \sim \psi_{14}$ are individually exhibited below the time axis of figure 3. Moreover, the squares of the real parts of the quasinormal frequencies $(\text{Re } \omega_n)^2$ are displayed as horizontal lines in the upper-right inset. The dashed lines represent the dominant modes with the same colors as those below the time axis, while the dotted lines denote other quasinormal modes. The quasinormal modes spread out beyond the potential valley by penetrating the potential barriers. It shows that, the smaller n is, the closer the quasinormal mode lives to the bottom of the valley, thus making it penetrate the potential barriers more difficult. Note that the coefficients c_n are strongly related to the transmission of the scalar perturbation penetrating the outer barrier, which implies that low-lying quasinormal modes have small values of c_n . For the quasinormal

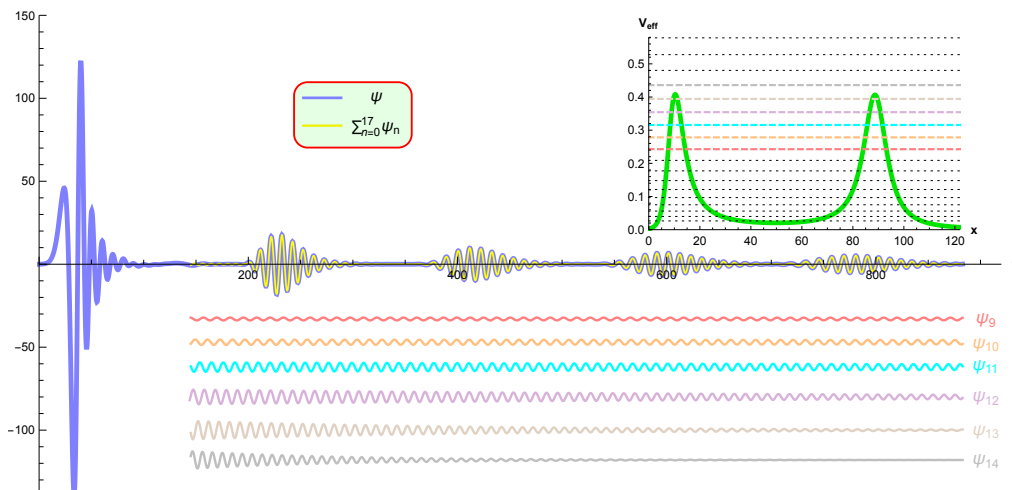


Figure 3. The upper-right inset shows the $l = 2$ effective potential of two well-separated peaks in the hairy black hole with $\alpha = 0.52$ and $Q = 1.0074$. The blue line denotes the observed time signal, which is obtained from numerical integration of eq. (2.7) with an initial Gaussian's packet near the outer peak. We take the observer to be sufficiently far away from the outer peak. Due to the double-peak structure, a sequence of echoes starts to appear after the primary signal, and can be well reconstructed from the quasinormal modes from $n = 0$ to $n = 17$ (yellow line). Below the time axis, we exhibit the waveform of the quasinormal modes from $n = 9$ to $n = 14$ individually, which dominate the reconstruction of the echoes. Additionally, $(\text{Re } \omega_n)^2$ of the quasinormal modes are plotted as horizontal lines in the inset. The smaller n is, the lower the horizontal line lies.

ω_n	C_n	ω_n	C_n
$n=0$ $\pm 0.1628 - 7.6180 \times 10^{-11}i$	$-4.950 \times 10^{-5} \mp 3.906 \times 10^{-5}i$	$n=9$ $\pm 0.4927 - 0.0001i$	$-0.174 \pm 0.395i$
$n=1$ $\pm 0.1997 - 1.0499 \times 10^{-9}i$	$4.065 \times 10^{-5} \mp 2.802 \times 10^{-4}i$	$n=10$ $\pm 0.5276 - 0.0002i$	$-0.825 \mp 0.134i$
$n=2$ $\pm 0.2369 - 7.8578 \times 10^{-9}i$	$8.205 \times 10^{-4} \mp 7.712 \times 10^{-4}i$	$n=11$ $\pm 0.5618 - 0.0007i$	$-0.088 \mp 1.564i$
$n=3$ $\pm 0.2740 - 4.3068 \times 10^{-8}i$	$0.002 \pm 0.002i$	$n=12$ $\pm 0.5952 - 0.0017i$	$2.727 \mp 0.651i$
$n=4$ $\pm 0.3111 - 1.9411 \times 10^{-7}i$	$-0.003 \pm 0.006i$	$n=13$ $\pm 0.6279 - 0.0036i$	$1.753 \pm 4.348i$
$n=5$ $\pm 0.3480 - 7.7389 \times 10^{-7}i$	$-0.019 \mp 0.002i$	$n=14$ $\pm 0.6603 - 0.0070i$	$-6.223 \pm 3.708i$
$n=6$ $\pm 0.3847 - 2.7912 \times 10^{-6}i$	$-0.012 \mp 0.045i$	$n=15$ $\pm 0.6932 - 0.0115i$	$-7.048 \mp 7.851i$
$n=7$ $\pm 0.4211 - 9.3216 \times 10^{-6}i$	$0.086 \mp 0.056i$	$n=16$ $\pm 0.7267 - 0.0169i$	$8.410 \mp 12.387i$
$n=8$ $\pm 0.4571 - 2.9323 \times 10^{-5}i$	$0.166 \pm 0.138i$	$n=17$ $\pm 0.7609 - 0.0227i$	$20.094 \pm 6.546i$

Table 1. The frequency ω_n of the quasinormal modes of $l = 2$ for a scalar field perturbation in the hairy black hole with $\alpha = 0.52$ and $Q = 1.0074$. The coefficient c_n , which controls the contribution from the corresponding quasinormal mode to the echoes in figure 3, is obtained from eq. (2.18). As n grows, the modulus of c_n becomes larger. Since the initial data is real, each pair of coefficients c_n are complex conjugate, leading to the real waveform of the quasinormal modes ψ_n .

modes $\psi_{n < 9}$, the coefficients $c_{n < 9}$ are so small that their contributions to the echoes can be neglected. On the other hand, the frequency of the high-lying modes $\psi_{n > 14}$ attains a large negative imaginary part, providing a prominent exponentially damping factor for the time signal.

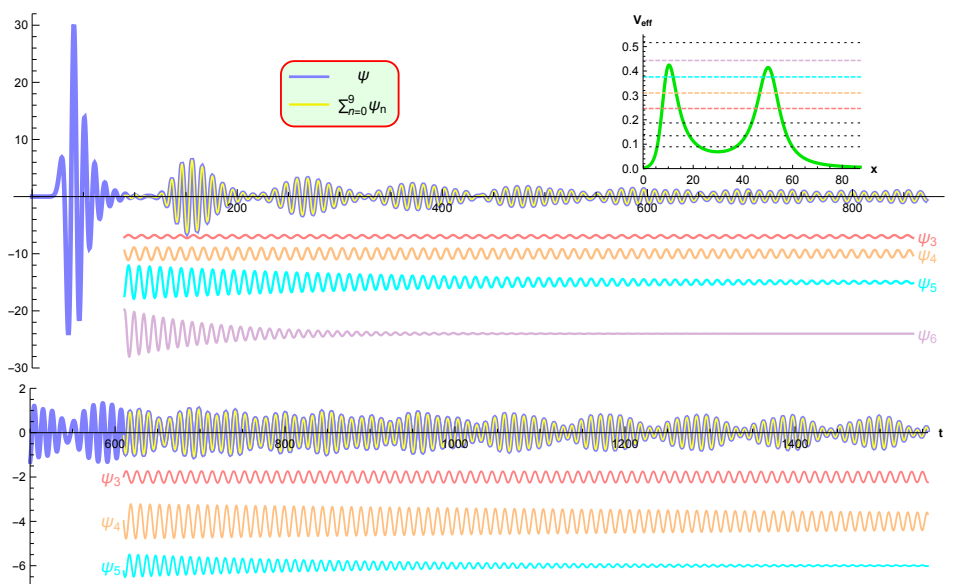


Figure 4. Exact numerical (blue lines) and reconstructed (yellow lines) waveforms ψ , and the dominant quasinormal modes received by a distant observer in the hairy black hole with $\alpha = 0.6$ and $Q = 1.0192$. Compared to figure 3, the effective potential has a smaller valley between two peaks, leading to fewer quasinormal modes (see horizontal lines, representing $(\text{Re } \omega_n)^2$ of quasinormal modes, in the inset). In the upper panel, the echoes are observed after the primary signal and disappear after some time. The lower panel shows the later behavior of the waveform. Interestingly, the echoes reoccur after the quasinormal mode ψ_5 is damped away. Specifically, the superposition of the quasinormal modes ψ_3 and ψ_4 produce the reoccurring echoes at the later time.

In figure 4, we display the numerically computed and reconstructed waveforms at a position far away from the outer peak in the hairy black hole solution with $\alpha = 0.6$ and $Q = 1.0192$, where the effective potential has a smaller valley than that of figure 3. In addition, the dominant quasinormal modes of the waveform ψ are also exhibited below the time axis. Unlike figure 3, we observe that there exists a time regime (roughly between 700 and 1000), in which echoes overlaps, and echo signals can be hardly identified. Interestingly, after the quasinormal mode ψ_5 becomes negligible, the echoes composed of the low-lying modes ψ_3 and ψ_4 reappear. Moreover, the frequency ω_n and the coefficient c_n of the quasinormal modes $\psi_{n \leq 9}$ are given in table 2. Compared to figure 3 and table 1, we find that fewer quasinormal modes are available to reconstruct the waveform due to a smaller potential valley [83]. In fact, as shown in the inset of figure 4, the quasinormal modes get farther apart as the potential valley becomes narrower and shallower.

3.3 Adjacent double-peak potential

Finally, we consider the hairy black hole solutions with the double-peak effective potential, where the separation between the peaks L is comparable to the Compton wavelength of the perturbations. Unlike the wormhole-like potential, the geometric optics approximation fails, and hence the time delay between the echoes can be larger than $2L$. Furthermore,

	ω_n	c_n		ω_n	c_n
$n=0$	$\pm 0.2990 - 6.6394 \times 10^{-8}i$	$-8.401 \times 10^{-5} \pm 2.133 \times 10^{-4}i$	$n=5$	$\pm 0.6129 - 0.0034i$	$0.897 \pm 1.817i$
$n=1$	$\pm 0.3667 - 1.3021 \times 10^{-6}i$	$-0.002 \mp 0.003i$	$n=6$	$\pm 0.6658 - 0.0110i$	$-5.460 \mp 1.547i$
$n=2$	$\pm 0.4327 - 1.4037 \times 10^{-5}i$	$0.027 \pm 0.007i$	$n=7$	$\pm 0.7190 - 0.0246i$	$11.431 \mp 9.173i$
$n=3$	$\pm 0.4963 - 0.0001i$	$-0.128 \pm 0.067i$	$n=8$	$\pm 0.7748 - 0.0421i$	$5.328 \pm 38.268i$
$n=4$	$\pm 0.5567 - 0.0007i$	$0.184 \mp 0.573i$	$n=9$	$\pm 0.8334 - 0.0612i$	$-98.389 \mp 39.720i$

Table 2. The frequency ω_n and the coefficient c_n of the quasinormal modes of $l = 2$ for a scalar field perturbation in the hairy black hole with $\alpha = 0.6$ and $Q = 1.0192$. Compared to table 1, fewer quasinormal modes are available to reconstruct the waveform in figure 4.

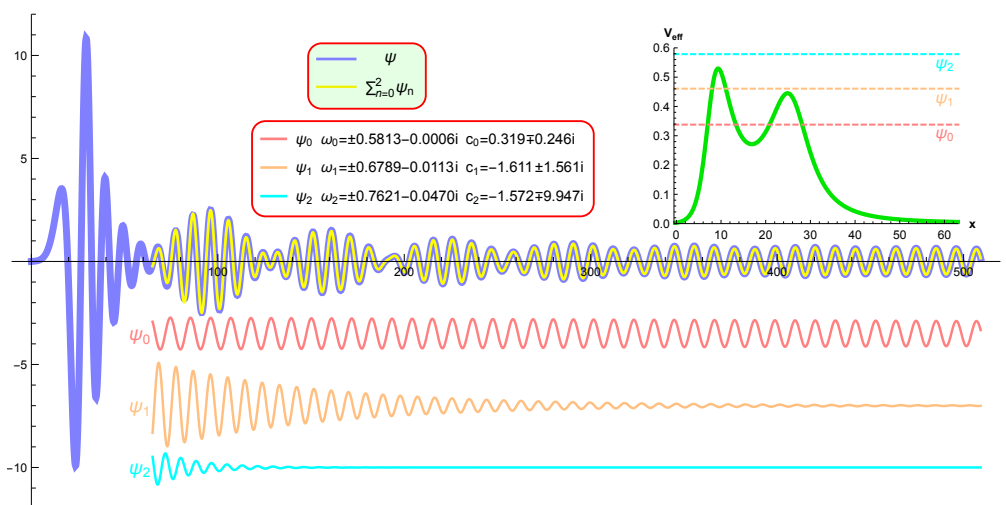


Figure 5. Numerical (blue line) and reconstructed (yellow line) waveforms ψ excited by a Gaussian perturbation near the outer potential peak in the hairy black hole with $\alpha = 0.8$ and $Q = 1.0514$. The observer is far away from the outer peak. Compared to figures 3 and 4, the effective potential has a significantly shallower and narrower valley. Therefore, only three quasinormal modes, namely ψ_0 , ψ_1 and ψ_2 , are needed to reconstruct the waveform after the primary signal is received. The superposition of these quasinormal modes leads to the observed echoes. Moreover, since the geometric optics approximation is invalid, the time delay between the echoes is obtained from the real parts of the quasinormal frequencies instead of the distance between the peaks. The dashed horizontal lines in the inset represent $(\text{Re } \omega_n)^2$ of ψ_0 , ψ_1 and ψ_2 , indicating that ψ_0 is trapped near the bottom of the potential valley and therefore a long-lived mode. After ψ_1 and ψ_2 are damped away, the waveform ψ is only determined by the long-lived mode ψ_0 , and hence has a sinusoid tail instead of echoes.

albeit there always exist long-lived modes trapped at the potential valley, the number of the long-lived modes decreases as L decreases [83]. In [83], we also found that, near the smaller local maximum of the potential, there appear sub-long-lived modes, which could play an important role in the late-time waveform when the contribution from the long-lived modes is suppressed by their small tunneling rates through the potential barriers.

In figure 5, we investigate the waveform of a scalar perturbation propagating in the double-peak effective potential of the hairy black hole with $\alpha = 0.8$ and $Q = 1.0514$, where

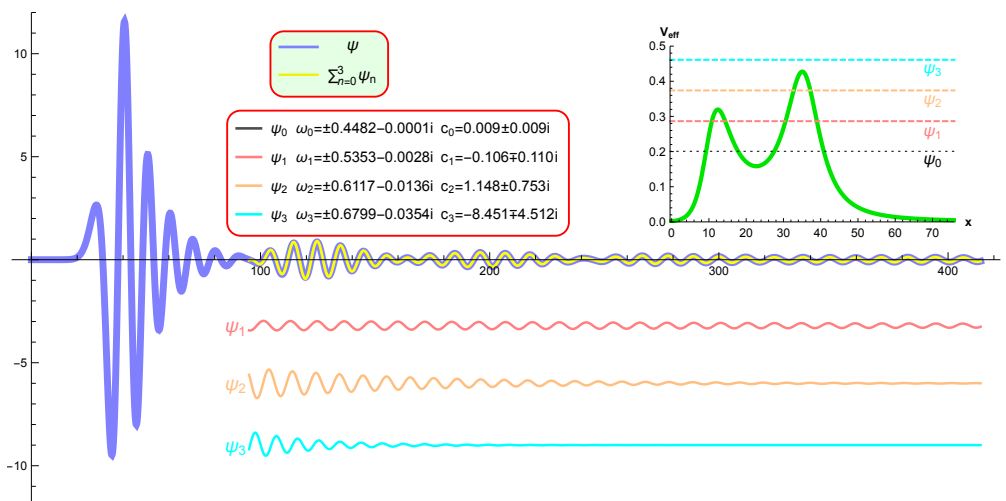


Figure 6. Numerical (blue line) and reconstructed (yellow line) waveforms ψ excited by a Gaussian perturbation near the outer potential peak in the hairy black hole with $\alpha = 0.7$ and $Q = 1.0340$, which has a higher outer potential barrier than in figure 5. The higher outer potential barrier reduces the transmission rate of the perturbation through the barrier. As a result, the long-lived mode ψ_0 is negligible, and the sub-long-lived mode ψ_1 trapped at the smaller local maximum of the potential determines the late-time sinusoid tail, which has a much smaller amplitude and a large decay rate than that in figure 5. In addition, there appears only one distinguishable echo, which mainly consists of the quasinormal modes ψ_1 , ψ_2 and ψ_3 .

the inner barrier is higher than the outer one. After the primary signal, one observes three distinct echoes followed by an apparent sinusoid. Since a shallow potential valley gives rise to fewer quasinormal modes [83], the late-time waveform ψ can be well reconstructed by only three lowest-lying modes $\psi_{n \leq 2}$. Moreover, one can read off the echo period $T \approx 64.38$ from the quasinormal frequencies ω_0 , ω_1 and ω_2 via eq. (2.19). Therefore, the echoes are separated by a distance $T \approx 64.38$, which is larger than $2L \approx 31.10$. In the inset, $(\text{Re } \omega_n)^2$ of the quasinormal modes $\psi_{n \leq 2}$ are displayed as dashed horizontal lines. It shows that the $n = 0$ quasinormal mode lives at the bottom of the potential valley and is a long-lived state with a very small imaginary part of the quasinormal frequency. Additionally, ψ_1 is a sub-long-lived mode that lives near the smaller local maximum of the double-peak potential. The superposition of ψ_0 , ψ_1 and ψ_2 generates the first echo, whereas the following echoes are mainly determined by ψ_0 and ψ_1 . After the echo signals, only the long-lived mode ψ_0 remains, which results in a long sinusoid tail. It is worth emphasizing that the amplitude of the tail is much larger than that in the single-peak case since the imaginary part of ω_0 is roughly 100 times smaller.

To illustrate the effect of the outer potential barrier on the received signals, we consider the hairy black hole with $\alpha = 0.7$ and $Q = 1.0340$, whose effective potential has a higher outer potential barrier than that in figure 5. In fact, as the height of the outer potential barrier increases, perturbations escape from the potential valley to a distant observer more difficultly. As expected, figure 6 shows that the late time signal detected by a distant observer is dimmer than that in figure 5. Specifically, the dashed horizontal lines in the inset

indicate that the quasinormal modes ψ_0 and ψ_1 are long-lived and sub-long-lived modes trapped at the minimum and the smaller local maximum of the potential, respectively. Due to the small transmission rate through the high outer barrier, the long-lived mode ψ_0 has the negligibly small coefficient c_0 and thus contributes little to the late-time signal. Consequently, the late-time waveform is primarily controlled by the sub-long-lived mode ψ_1 , which has smaller modulus of the coefficient c_1 and decays faster than the long-lived mode ψ_0 in figure 5, hence leading to fewer echoes and a smaller sinusoid tail.

4 Conclusions

In this paper, we first studied hairy black holes in the EMS model, where the scalar field is minimally coupled to the gravity sector and non-minimally coupled to the electromagnetic field. It showed that the effective potential of scalar perturbations can possess a single peak or two peaks depending on the black hole parameters. Moreover, for the double-peak potential, the separation between the peaks can be significantly larger or comparable to the Compton wavelength of the perturbations. Considering an initial Gaussian perturbation near the (outer) potential peak, the evolution of the time-dependent scalar perturbation was then computed in several hairy black holes to investigate how the peak structure affects the late-time waveform of the perturbation received by an observer far away from the (outer) peak. Specifically, the waveform was obtained by numerically solving the partial differential equation (2.7). To find the frequency content of the waveform, we also used eq. (2.17) to reconstruct the waveform with the associated quasinormal modes. Our results showed that the numerical and reconstructed waveforms are in excellent agreement.

After relaxation of the initial perturbation, the observer first detects a primary signal, which is the reflected wave off the (outer) potential peak and hence essentially controlled by the quasinormal modes associated with the (outer) peak. If there is no inner peak, the late-time waveform after the primary signal is an exponentially decaying sinusoid, which is the fundamental quasinormal mode. On the other hand, the late-time waveform in a double-peak potential is mostly determined by the long-lived and sub-long-lived quasinormal modes, which live near the minimum and the smaller local maximum of the potential, respectively. When the distance between the peaks is large, there exist a number of long-lived and sub-long-lived modes, which produce a train of decaying echo pulses observed in figures 3 and 4. Remarkably, if the number of long-lived modes is small enough, echo signals can disappear for some time and then reappear (see figure 4). When the potential peaks are close enough, there exist only one long-lived mode and one sub-long-lived mode. The superposition of the long-lived, sub-long-lived and other low-lying modes give a few observed echoes following the primary signal (see figures 5 and 6). For a low outer potential barrier, the long-lived mode dominates the waveform of the perturbation after other modes are damped away, producing a very slowly decaying sinusoid tail (see figure 5). For a high outer potential barrier, the long-lived mode is suppressed, and the sub-long-lived is then responsible for the sinusoid tail of the waveform, which decays faster and has a much smaller amplitude (see figure 6).

For spherically symmetric hairy black holes, the connection between double-peak effective potentials and the existence of multiple photon spheres outside the event horizon has been discussed in [83]. The late-time waveform excited by a scalar perturbation may provide a smoking gun for the detection of black holes with multiple photon spheres. It will be of great interest if our analysis can be generalized beyond spherical symmetry and for more general black hole spacetimes.

Acknowledgments

We are grateful to Yiqian Chen and Xin Jiang for useful discussions and valuable comments. This work is supported in part by NSFC (Grant No. 12105191, 11947225 and 11875196). Houwen Wu is supported by the International Visiting Program for Excellent Young Scholars of Sichuan University.

Open Access. This article is distributed under the terms of the Creative Commons Attribution License ([CC-BY 4.0](https://creativecommons.org/licenses/by/4.0/)), which permits any use, distribution and reproduction in any medium, provided the original author(s) and source are credited.

References

- [1] LIGO SCIENTIFIC and VIRGO collaborations, *Observation of Gravitational Waves from a Binary Black Hole Merger*, *Phys. Rev. Lett.* **116** (2016) 061102 [[arXiv:1602.03837](https://arxiv.org/abs/1602.03837)] [[INSPIRE](#)].
- [2] EVENT HORIZON TELESCOPE collaboration, *First M87 Event Horizon Telescope Results. I. The Shadow of the Supermassive Black Hole*, *Astrophys. J. Lett.* **875** (2019) L1 [[arXiv:1906.11238](https://arxiv.org/abs/1906.11238)] [[INSPIRE](#)].
- [3] EVENT HORIZON TELESCOPE collaboration, *First M87 Event Horizon Telescope Results. II. Array and Instrumentation*, *Astrophys. J. Lett.* **875** (2019) L2 [[arXiv:1906.11239](https://arxiv.org/abs/1906.11239)] [[INSPIRE](#)].
- [4] EVENT HORIZON TELESCOPE collaboration, *First M87 Event Horizon Telescope Results. III. Data Processing and Calibration*, *Astrophys. J. Lett.* **875** (2019) L3 [[arXiv:1906.11240](https://arxiv.org/abs/1906.11240)] [[INSPIRE](#)].
- [5] EVENT HORIZON TELESCOPE collaboration, *First M87 Event Horizon Telescope Results. IV. Imaging the Central Supermassive Black Hole*, *Astrophys. J. Lett.* **875** (2019) L4 [[arXiv:1906.11241](https://arxiv.org/abs/1906.11241)] [[INSPIRE](#)].
- [6] EVENT HORIZON TELESCOPE collaboration, *First M87 Event Horizon Telescope Results. V. Physical Origin of the Asymmetric Ring*, *Astrophys. J. Lett.* **875** (2019) L5 [[arXiv:1906.11242](https://arxiv.org/abs/1906.11242)] [[INSPIRE](#)].
- [7] EVENT HORIZON TELESCOPE collaboration, *First M87 Event Horizon Telescope Results. VI. The Shadow and Mass of the Central Black Hole*, *Astrophys. J. Lett.* **875** (2019) L6 [[arXiv:1906.11243](https://arxiv.org/abs/1906.11243)] [[INSPIRE](#)].
- [8] H.-P. Nollert, *TOPICAL REVIEW: Quasinormal modes: the characteristic ‘sound’ of black holes and neutron stars*, *Class. Quant. Grav.* **16** (1999) R159 [[INSPIRE](#)].
- [9] E. Berti, V. Cardoso, J.A. Gonzalez and U. Sperhake, *Mining information from binary black hole mergers: A comparison of estimation methods for complex exponentials in noise*, *Phys. Rev. D* **75** (2007) 124017 [[gr-qc/0701086](https://arxiv.org/abs/gr-qc/0701086)] [[INSPIRE](#)].

- [10] V. Cardoso, E. Franzin and P. Pani, *Is the gravitational-wave ringdown a probe of the event horizon?*, *Phys. Rev. Lett.* **116** (2016) 171101 [Erratum *ibid.* **117** (2016) 089902] [[arXiv:1602.07309](#)] [[INSPIRE](#)].
- [11] R.H. Price and G. Khanna, *Gravitational wave sources: reflections and echoes*, *Class. Quant. Grav.* **34** (2017) 225005 [[arXiv:1702.04833](#)] [[INSPIRE](#)].
- [12] M. Giesler, M. Isi, M.A. Scheel and S. Teukolsky, *Black Hole Ringdown: The Importance of Overtones*, *Phys. Rev. X* **9** (2019) 041060 [[arXiv:1903.08284](#)] [[INSPIRE](#)].
- [13] J.P.S. Lemos and O.B. Zaslavskii, *Black hole mimickers: Regular versus singular behavior*, *Phys. Rev. D* **78** (2008) 024040 [[arXiv:0806.0845](#)] [[INSPIRE](#)].
- [14] P.V.P. Cunha, J.A. Font, C. Herdeiro, E. Radu, N. Sanchis-Gual and M. Zilhão, *Lensing and dynamics of ultracompact bosonic stars*, *Phys. Rev. D* **96** (2017) 104040 [[arXiv:1709.06118](#)] [[INSPIRE](#)].
- [15] P.V.P. Cunha and C.A.R. Herdeiro, *Shadows and strong gravitational lensing: a brief review*, *Gen. Rel. Grav.* **50** (2018) 42 [[arXiv:1801.00860](#)] [[INSPIRE](#)].
- [16] R. Shaikh, P. Banerjee, S. Paul and T. Sarkar, *A novel gravitational lensing feature by wormholes*, *Phys. Lett. B* **789** (2019) 270 [Erratum *ibid.* **791** (2019) 422] [[arXiv:1811.08245](#)] [[INSPIRE](#)].
- [17] D.-C. Dai and D. Stojkovic, *Observing a Wormhole*, *Phys. Rev. D* **100** (2019) 083513 [[arXiv:1910.00429](#)] [[INSPIRE](#)].
- [18] H. Huang and J. Yang, *Charged Ellis Wormhole and Black Bounce*, *Phys. Rev. D* **100** (2019) 124063 [[arXiv:1909.04603](#)] [[INSPIRE](#)].
- [19] J.H. Simonetti, M.J. Kavic, D. Minic, D. Stojkovic and D.-C. Dai, *Sensitive searches for wormholes*, *Phys. Rev. D* **104** (2021) L081502 [[arXiv:2007.12184](#)] [[INSPIRE](#)].
- [20] M. Wielgus, J. Horak, F. Vincent and M. Abramowicz, *Reflection-asymmetric wormholes and their double shadows*, *Phys. Rev. D* **102** (2020) 084044 [[arXiv:2008.10130](#)] [[INSPIRE](#)].
- [21] J. Yang and H. Huang, *Trapping horizons of the evolving charged wormhole and black bounce*, *Phys. Rev. D* **104** (2021) 084005 [[arXiv:2104.11134](#)] [[INSPIRE](#)].
- [22] C. Bambi and D. Stojkovic, *Astrophysical Wormholes*, *Universe* **7** (2021) 136 [[arXiv:2105.00881](#)] [[INSPIRE](#)].
- [23] J. Peng, M. Guo and X.-H. Feng, *Observational signature and additional photon rings of an asymmetric thin-shell wormhole*, *Phys. Rev. D* **104** (2021) 124010 [[arXiv:2102.05488](#)] [[INSPIRE](#)].
- [24] P. Bueno, P.A. Cano, F. Goelen, T. Hertog and B. Vercknocke, *Echoes of Kerr-like wormholes*, *Phys. Rev. D* **97** (2018) 024040 [[arXiv:1711.00391](#)] [[INSPIRE](#)].
- [25] R.A. Konoplya, Z. Stuchlík and A. Zhidenko, *Echoes of compact objects: new physics near the surface and matter at a distance*, *Phys. Rev. D* **99** (2019) 024007 [[arXiv:1810.01295](#)] [[INSPIRE](#)].
- [26] Y.-T. Wang, J. Zhang and Y.-S. Piao, *Primordial gravastar from inflation*, *Phys. Lett. B* **795** (2019) 314 [[arXiv:1810.04885](#)] [[INSPIRE](#)].
- [27] Y.-T. Wang, Z.-P. Li, J. Zhang, S.-Y. Zhou and Y.-S. Piao, *Are gravitational wave ringdown echoes always equal-interval?*, *Eur. Phys. J. C* **78** (2018) 482 [[arXiv:1802.02003](#)] [[INSPIRE](#)].

- [28] V. Cardoso and P. Pani, *Testing the nature of dark compact objects: a status report*, *Living Rev. Rel.* **22** (2019) 4 [[arXiv:1904.05363](#)] [[INSPIRE](#)].
- [29] J.T. Gálvez Gherzi, A.V. Frolov and D.A. Dobre, *Echoes from the scattering of wavepackets on wormholes*, *Class. Quant. Grav.* **36** (2019) 135006 [[arXiv:1901.06625](#)] [[INSPIRE](#)].
- [30] H. Liu, P. Liu, Y. Liu, B. Wang and J.-P. Wu, *Echoes from phantom wormholes*, *Phys. Rev. D* **103** (2021) 024006 [[arXiv:2007.09078](#)] [[INSPIRE](#)].
- [31] M.-Y. Ou, M.-Y. Lai and H. Huang, *Echoes from asymmetric wormholes and black bounce*, *Eur. Phys. J. C* **82** (2022) 452 [[arXiv:2111.13890](#)] [[INSPIRE](#)].
- [32] J. Abedi, H. Dykaar and N. Afshordi, *Echoes from the Abyss: Tentative evidence for Planck-scale structure at black hole horizons*, *Phys. Rev. D* **96** (2017) 082004 [[arXiv:1612.00266](#)] [[INSPIRE](#)].
- [33] J. Abedi, H. Dykaar and N. Afshordi, *Echoes from the Abyss: The Holiday Edition!*, [arXiv:1701.03485](#) [[INSPIRE](#)].
- [34] R. Dey, S. Biswas and S. Chakraborty, *Ergoregion instability and echoes for braneworld black holes: Scalar, electromagnetic, and gravitational perturbations*, *Phys. Rev. D* **103** (2021) 084019 [[arXiv:2010.07966](#)] [[INSPIRE](#)].
- [35] Y. Yang, D. Liu, Z. Xu, Y. Xing, S. Wu and Z.-W. Long, *Echoes of novel black-bounce spacetimes*, *Phys. Rev. D* **104** (2021) 104021 [[arXiv:2107.06554](#)] [[INSPIRE](#)].
- [36] S.H. Völkel and K.D. Kokkotas, *Ultra Compact Stars: Reconstructing the Perturbation Potential*, *Class. Quant. Grav.* **34** (2017) 175015 [[arXiv:1704.07517](#)] [[INSPIRE](#)].
- [37] Z. Mark, A. Zimmerman, S.M. Du and Y. Chen, *A recipe for echoes from exotic compact objects*, *Phys. Rev. D* **96** (2017) 084002 [[arXiv:1706.06155](#)] [[INSPIRE](#)].
- [38] Q. Wang, N. Oshita and N. Afshordi, *Echoes from Quantum Black Holes*, *Phys. Rev. D* **101** (2020) 024031 [[arXiv:1905.00446](#)] [[INSPIRE](#)].
- [39] K. Saraswat and N. Afshordi, *Quantum Nature of Black Holes: Fast Scrambling versus Echoes*, *JHEP* **04** (2020) 136 [[arXiv:1906.02653](#)] [[INSPIRE](#)].
- [40] R. Dey, S. Chakraborty and N. Afshordi, *Echoes from braneworld black holes*, *Phys. Rev. D* **101** (2020) 104014 [[arXiv:2001.01301](#)] [[INSPIRE](#)].
- [41] N. Oshita, D. Tsuna and N. Afshordi, *Quantum Black Hole Seismology I: Echoes, Ergospheres, and Spectra*, *Phys. Rev. D* **102** (2020) 024045 [[arXiv:2001.11642](#)] [[INSPIRE](#)].
- [42] S. Chakraborty, E. Maggio, A. Mazumdar and P. Pani, *Implications of the quantum nature of the black hole horizon on the gravitational-wave ringdown*, [arXiv:2202.09111](#) [[INSPIRE](#)].
- [43] H. Liu, W.-L. Qian, Y. Liu, J.-P. Wu, B. Wang and R.-H. Yue, *Alternative mechanism for black hole echoes*, *Phys. Rev. D* **104** (2021) 044012 [[arXiv:2104.11912](#)] [[INSPIRE](#)].
- [44] K. Chakravarti, R. Ghosh and S. Sarkar, *Signature of nonuniform area quantization on black hole echoes*, *Phys. Rev. D* **105** (2022) 044046 [[arXiv:2112.10109](#)] [[INSPIRE](#)].
- [45] G. D’Amico and N. Kaloper, *Black hole echoes*, *Phys. Rev. D* **102** (2020) 044001 [[arXiv:1912.05584](#)] [[INSPIRE](#)].
- [46] H.-S. Liu, Z.-F. Mai, Y.-Z. Li and H. Lü, *Quasi-topological Electromagnetism: Dark Energy, Dyonic Black Holes, Stable Photon Spheres and Hidden Electromagnetic Duality*, *Sci. China Phys. Mech. Astron.* **63** (2020) 240411 [[arXiv:1907.10876](#)] [[INSPIRE](#)].

- [47] H. Huang, M.-Y. Ou, M.-Y. Lai and H. Lü, *Echoes from classical black holes*, *Phys. Rev. D* **105** (2022) 104049 [[arXiv:2112.14780](#)] [[INSPIRE](#)].
- [48] C. de Rham, G. Gabadadze and A.J. Tolley, *Resummation of Massive Gravity*, *Phys. Rev. Lett.* **106** (2011) 231101 [[arXiv:1011.1232](#)] [[INSPIRE](#)].
- [49] J. Zhang and S.-Y. Zhou, *Can the graviton have a large mass near black holes?*, *Phys. Rev. D* **97** (2018) 081501 [[arXiv:1709.07503](#)] [[INSPIRE](#)].
- [50] R. Dong and D. Stojkovic, *Gravitational wave echoes from black holes in massive gravity*, *Phys. Rev. D* **103** (2021) 024058 [[arXiv:2011.04032](#)] [[INSPIRE](#)].
- [51] C.A.R. Herdeiro, E. Radu, N. Sanchis-Gual and J.A. Font, *Spontaneous Scalarization of Charged Black Holes*, *Phys. Rev. Lett.* **121** (2018) 101102 [[arXiv:1806.05190](#)] [[INSPIRE](#)].
- [52] R.A. Konoplya and A. Zhidenko, *Analytical representation for metrics of scalarized Einstein-Maxwell black holes and their shadows*, *Phys. Rev. D* **100** (2019) 044015 [[arXiv:1907.05551](#)] [[INSPIRE](#)].
- [53] P. Wang, H. Wu and H. Yang, *Scalarized Einstein-Born-Infeld black holes*, *Phys. Rev. D* **103** (2021) 104012 [[arXiv:2012.01066](#)] [[INSPIRE](#)].
- [54] G. Guo, P. Wang, H. Wu and H. Yang, *Scalarized Einstein-Maxwell-scalar black holes in anti-de Sitter spacetime*, *Eur. Phys. J. C* **81** (2021) 864 [[arXiv:2102.04015](#)] [[INSPIRE](#)].
- [55] G. Guo, P. Wang, H. Wu and H. Yang, *Thermodynamics and phase structure of an Einstein-Maxwell-scalar model in extended phase space*, *Phys. Rev. D* **105** (2022) 064069 [[arXiv:2107.04467](#)] [[INSPIRE](#)].
- [56] W. Israel, *Event horizons in static vacuum space-times*, *Phys. Rev.* **164** (1967) 1776 [[INSPIRE](#)].
- [57] B. Carter, *Axissymmetric Black Hole Has Only Two Degrees of Freedom*, *Phys. Rev. Lett.* **26** (1971) 331 [[INSPIRE](#)].
- [58] R. Ruffini and J.A. Wheeler, *Introducing the black hole*, *Phys. Today* **24** (1971) 30 [[INSPIRE](#)].
- [59] P.G.S. Fernandes, C.A.R. Herdeiro, A.M. Pombo, E. Radu and N. Sanchis-Gual, *Spontaneous Scalarisation of Charged Black Holes: Coupling Dependence and Dynamical Features*, *Class. Quant. Grav.* **36** (2019) 134002 [Erratum *ibid.* **37** (2020) 049501] [[arXiv:1902.05079](#)] [[INSPIRE](#)].
- [60] P.G.S. Fernandes, C.A.R. Herdeiro, A.M. Pombo, E. Radu and N. Sanchis-Gual, *Charged black holes with axionic-type couplings: Classes of solutions and dynamical scalarization*, *Phys. Rev. D* **100** (2019) 084045 [[arXiv:1908.00037](#)] [[INSPIRE](#)].
- [61] J.L. Blázquez-Salcedo, C.A.R. Herdeiro, J. Kunz, A.M. Pombo and E. Radu, *Einstein-Maxwell-scalar black holes: the hot, the cold and the bald*, *Phys. Lett. B* **806** (2020) 135493 [[arXiv:2002.00963](#)] [[INSPIRE](#)].
- [62] D.-C. Zou and Y.S. Myung, *Scalarized charged black holes with scalar mass term*, *Phys. Rev. D* **100** (2019) 124055 [[arXiv:1909.11859](#)] [[INSPIRE](#)].
- [63] P.G.S. Fernandes, *Einstein-Maxwell-scalar black holes with massive and self-interacting scalar hair*, *Phys. Dark Univ.* **30** (2020) 100716 [[arXiv:2003.01045](#)] [[INSPIRE](#)].
- [64] Y. Peng, *Scalarization of horizonless reflecting stars: neutral scalar fields non-minimally coupled to Maxwell fields*, *Phys. Lett. B* **804** (2020) 135372 [[arXiv:1912.11989](#)] [[INSPIRE](#)].
- [65] Y.S. Myung and D.-C. Zou, *Instability of Reissner-Nordström black hole in Einstein-Maxwell-scalar theory*, *Eur. Phys. J. C* **79** (2019) 273 [[arXiv:1808.02609](#)] [[INSPIRE](#)].

- [66] Y.S. Myung and D.-C. Zou, *Stability of scalarized charged black holes in the Einstein-Maxwell-Scalar theory*, *Eur. Phys. J. C* **79** (2019) 641 [[arXiv:1904.09864](#)] [[INSPIRE](#)].
- [67] D.-C. Zou and Y.S. Myung, *Radial perturbations of the scalarized black holes in Einstein-Maxwell-conformally coupled scalar theory*, *Phys. Rev. D* **102** (2020) 064011 [[arXiv:2005.06677](#)] [[INSPIRE](#)].
- [68] Y.S. Myung and D.-C. Zou, *Onset of rotating scalarized black holes in Einstein-Chern-Simons-Scalar theory*, *Phys. Lett. B* **814** (2021) 136081 [[arXiv:2012.02375](#)] [[INSPIRE](#)].
- [69] Z.-F. Mai and R.-Q. Yang, *Stability analysis of a charged black hole with a nonlinear complex scalar field*, *Phys. Rev. D* **104** (2021) 044008 [[arXiv:2101.00026](#)] [[INSPIRE](#)].
- [70] D. Astefanesei, C. Herdeiro, J. Oliveira and E. Radu, *Higher dimensional black hole scalarization*, *JHEP* **09** (2020) 186 [[arXiv:2007.04153](#)] [[INSPIRE](#)].
- [71] Y.S. Myung and D.-C. Zou, *Quasinormal modes of scalarized black holes in the Einstein-Maxwell-Scalar theory*, *Phys. Lett. B* **790** (2019) 400 [[arXiv:1812.03604](#)] [[INSPIRE](#)].
- [72] J. Luis Blázquez-Salcedo, C.A.R. Herdeiro, S. Kahlen, J. Kunz, A.M. Pombo and E. Radu, *Quasinormal modes of hot, cold and bald Einstein-Maxwell-scalar black holes*, *Eur. Phys. J. C* **81** (2021) 155 [[arXiv:2008.11744](#)] [[INSPIRE](#)].
- [73] Y.S. Myung and D.-C. Zou, *Scalarized charged black holes in the Einstein-Maxwell-Scalar theory with two U(1) fields*, *Phys. Lett. B* **811** (2020) 135905 [[arXiv:2009.05193](#)] [[INSPIRE](#)].
- [74] Y.S. Myung and D.-C. Zou, *Scalarized black holes in the Einstein-Maxwell-scalar theory with a quasitopological term*, *Phys. Rev. D* **103** (2021) 024010 [[arXiv:2011.09665](#)] [[INSPIRE](#)].
- [75] H. Guo, X.-M. Kuang, E. Papantonopoulos and B. Wang, *Horizon curvature and spacetime structure influences on black hole scalarization*, *Eur. Phys. J. C* **81** (2021) 842 [[arXiv:2012.11844](#)] [[INSPIRE](#)].
- [76] Y. Brihaye, B. Hartmann, N.P. Aprile and J. Urrestilla, *Scalarization of asymptotically anti-de Sitter black holes with applications to holographic phase transitions*, *Phys. Rev. D* **101** (2020) 124016 [[arXiv:1911.01950](#)] [[INSPIRE](#)].
- [77] Y. Brihaye, C. Herdeiro and E. Radu, *Black Hole Spontaneous Scalarisation with a Positive Cosmological Constant*, *Phys. Lett. B* **802** (2020) 135269 [[arXiv:1910.05286](#)] [[INSPIRE](#)].
- [78] C.-Y. Zhang, P. Liu, Y. Liu, C. Niu and B. Wang, *Dynamical charged black hole spontaneous scalarization in anti-de Sitter spacetimes*, *Phys. Rev. D* **104** (2021) 084089 [[arXiv:2103.13599](#)] [[INSPIRE](#)].
- [79] C. de Rham and J. Zhang, *Perturbations of stealth black holes in degenerate higher-order scalar-tensor theories*, *Phys. Rev. D* **100** (2019) 124023 [[arXiv:1907.00699](#)] [[INSPIRE](#)].
- [80] Y. Xie, J. Zhang, H.O. Silva, C. de Rham, H. Witek and N. Yunes, *Square Peg in a Circular Hole: Choosing the Right Ansatz for Isolated Black Holes in Generic Gravitational Theories*, *Phys. Rev. Lett.* **126** (2021) 241104 [[arXiv:2103.03925](#)] [[INSPIRE](#)].
- [81] Q. Gan, P. Wang, H. Wu and H. Yang, *Photon spheres and spherical accretion image of a hairy black hole*, *Phys. Rev. D* **104** (2021) 024003 [[arXiv:2104.08703](#)] [[INSPIRE](#)].
- [82] Q. Gan, P. Wang, H. Wu and H. Yang, *Photon ring and observational appearance of a hairy black hole*, *Phys. Rev. D* **104** (2021) 044049 [[arXiv:2105.11770](#)] [[INSPIRE](#)].

- [83] G. Guo, P. Wang, H. Wu and H. Yang, *Quasinormal Modes of Black Holes with Multiple Photon Spheres*, [arXiv:2112.14133](#) [INSPIRE].
- [84] N. Andersson, *Evolving test fields in a black hole geometry*, *Phys. Rev. D* **55** (1997) 468 [[gr-qc/9607064](#)] [INSPIRE].
- [85] V. Cardoso, S. Hopper, C.F.B. Macedo, C. Palenzuela and P. Pani, *Gravitational-wave signatures of exotic compact objects and of quantum corrections at the horizon scale*, *Phys. Rev. D* **94** (2016) 084031 [[arXiv:1608.08637](#)] [INSPIRE].
- [86] V. Cardoso and P. Pani, *The observational evidence for horizons: from echoes to precision gravitational-wave physics*, [arXiv:1707.03021](#) [INSPIRE].
- [87] N. Sago, S. Isoyama and H. Nakano, *Fundamental Tone and Overtones of Quasinormal Modes in Ringdown Gravitational Waves: A Detailed Study in Black Hole Perturbation*, *Universe* **7** (2021) 357 [[arXiv:2108.13017](#)] [INSPIRE].
- [88] R.H. Price, *Nonspherical Perturbations of Relativistic Gravitational Collapse. II. Integer-Spin, Zero-Rest-Mass Fields*, *Phys. Rev. D* **5** (1972) 2439 [INSPIRE].
- [89] E.S.C. Ching, P.T. Leung, W.M. Suen and K. Young, *Late time tail of wave propagation on curved space-time*, *Phys. Rev. Lett.* **74** (1995) 2414 [[gr-qc/9410044](#)] [INSPIRE].